Int. J. Heat Mass Transfer. Vol. 36, No. 15, pp. 3783–3795, 1993
Printed in Great Britain

0017–9310/93 $6.00 + 0.00

Steady and oscillatory opposing mixed convection in a symmetrically heated vertical channel with a low-Prandtl number fluid

TSAI-SHOU CHANG and TSING-FA LIN

Department of Mechanical Engineering, Manufacturing and Thermal–Fluid Engineering Research Center, National Chiao Tung University, Hsinchu, Taiwan, R.O.C.

(*Received* 19 *June* 1992 *and in final form* 23 *February* 1993)

Abstract—Steady laminar and transient oscillatory mixed convection of a low Prandtl number fluid in a symmetrically heated vertical plane channel subject to an opposing buoyancy is investigated by solving the transient two-dimensional flow and energy equations. Results are particularly presented to illustrate the effects of buoyancy strength Gr/Re^2 and Reynolds number Re. At a fixed Reynolds number, the flow is steady and unidirectional for a long time for a very small Gr/Re^2. At a higher Gr/Re^2, steady flow reversal is noted. An oscillatory flow with a single fundamental frequency is found when Gr/Re^2 exceeds a critical value (which is about -1.2 with $Re = 500$). Flow asymmetry appears at a certain time instant. Further increasing the opposing buoyancy, a secondary fundamental frequency sets in and the flow is quasi-periodic. The effect of increasing the Reynolds number is to stabilize the flow. Besides, in the initial transient the larger Reynolds number results in a longer duration in which a number of symmetric cells oscillate longitudinally. Finally, the transition of various flow patterns can be clearly distinguished by noting a sudden change of the average Nusselt numbers.

INTRODUCTION

EXTENSIVE studies have been carried out in the literature for the mixed convection of air and water in both external and internal flows, as evident from the up-to-date reviews from Chen [1], Aung [2] and Gebhart *et al.* [3]. However, the mixed convection in low Prandtl number liquid metal flow is rarely investigated, in spite of its importance in the casting processes [4] and liquid metal-cooled fast breeder nuclear reactors [5]. This study intends to explore the detailed flow and thermal characteristics of a mixed convective liquid metal flow in a vertical plane channel under symmetric heating.

Early studies on the mixed convection in a vertical flat duct mainly focused on the buoyancy induced velocity distortion and the associated heat transfer in the steady laminar fully developed and developing flows. These include the results from Tao [6], Quintiere and Mueller [7], Yao [8], Chow *et al.* [9] and Aung and Worku [10, 11]. The reverse of a vertical forced channel flow by the strong buoyancy was examined by Cebeci *et al.* [12], Aung and Worku [13], Lavine [14], Ingham *et al.* [15–18], and Lavine *et al.* [19]. The reversed flow is known to be relatively unstable due to the existence of inflection points in the velocity profile, according to the boundary layer instability [20]. Unsteady mixed convection in a vertical pipe was treated by Shaddy [21]. Experimental investigation on the instability and transition of the mixed convection in vertical tube was conducted by Scheele *et al.* [22], Scheele and Hanratty [23], Lawrence and Chato [24], and Zeldin and Schmidt [25]. The above literature review indicates that mixed convection in air and water receives nearly all the attention.

Buoyancy-induced convection in a low-Prandtl fluid contained in enclosed cavities is found to be rather unstable and has been studied by a number of research groups such as Hurle *et al.* [26], Knuteson *et al.* [27] and Muller [28], to name just a few. There are only a few studies in the open literature dealing with the mixed convection channel flow of a low Prandtl number fluid.

In the present study, a detailed numerical simulation will be performed to unravel the steady and oscillatory flow and thermal characteristics in a forced flow of liquid metal through a vertical plane channel modified by an opposing buoyancy. The physical model under consideration and the coordinates chosen are depicted in Fig. 1. As shown in the figure, a parallel plane channel of wall thickness δ and inter-plate spacing b is oriented along the gravitational direction. The dimension of the channel walls perpendicular to the x–y plane is very large so that the flow can be considered as two-dimensional. A downward flow enters the channel at temperature T_e in the far upstream region, $x \to -\infty$. Initially, the flow and the confining walls are at the same uniform temperature T_e. At time = 0, uniform and equal heat fluxes are respectively imposed on the left and right walls over the finite length ($0 \leqslant x \leqslant l$) and maintained at these levels thereafter. Upstream and downstream of the heated section ($x \leqslant 0$ or $x \geqslant l$) the channel is well insulated. The flow is assumed to reach the fully developed state prior to moving into the region of

NOMENCLATURE

A	wall-to-fluid heat capacity ratio
b	channel width
$\vec{B}$	body force
c	complex wave speed
c_p	specific heat at constant pressure
g	gravitational acceleration
Gr	Grashof number
h	convection heat transfer coefficient
k	thermal conductivity of fluid
k_1	wave number
l, L	dimensional and dimensionless lengths of the directly heated section, respectively
Nu	Nusselt number
$\overline{Nu}$	average Nusselt number
$\overline{\overline{Nu}}$	effective heat transfer coefficient
p, P	dimensional and dimensionless pressures, respectively
p_m	dynamic (motion) pressure
Pe	Peclet number, $Re\,Pr$
Pr	Prandtl number
q''	heat flux
Re	Reynolds number
t	time
T	temperature
u, U	dimensional and dimensionless velocity in x-direction, respectively
v, V	dimensional and dimensionless velocity in y-direction, respectively
$\vec{V}$	velocity vector
$\hat{V}$	dimensionless velocity disturbance in Y-direction
x, y	Cartesian coordinates
X, Y	dimensionless Cartesian coordinates.

Greek symbols

α	thermal diffusivity
β	coefficient of volumetric thermal expansion
δ	thickness of the channel wall
ΔX	grid size in X-direction
$\Delta\tau$	time interval
θ	dimensionless temperature
$\hat{\theta}$	dimensionless temperature disturbance
ν	kinematic viscosity
ρ	density
τ	dimensionless time.

Subscripts

b	bulk quantity or basic flow quantity
e	entrance plane
i, j	indices in x- and y-directions
L	on the left wall
R	on the right wall
w	on wall
x	local quantity.

Superscripts

n	time step
*	predicted value.

significant heat transfer. Only buoyancy opposing flows will be examined since flow reversal frequently appears under this situation. Particular attention is paid to examining the unsteady oscillatory flow and heat transfer characteristics during the development of recirculating flow.

MATHEMATICAL FORMULATION

Basic nondimensional equations for the unsteady two-dimensional combined forced and free convection of a Boussinesq fluid through a vertical channel with the possible presence of flow recirculation are

$$\frac{\partial U}{\partial X}+\frac{\partial V}{\partial Y}=0 \tag{1}$$

$$\frac{\partial U}{\partial \tau}+U\frac{\partial U}{\partial X}+V\frac{\partial U}{\partial Y}=-\frac{\partial P}{\partial X}+\frac{Gr}{Re^2}\theta+\frac{1}{Re}\left[\frac{\partial^2 U}{\partial X^2}+\frac{\partial^2 U}{\partial Y^2}\right] \tag{2}$$

$$\frac{\partial V}{\partial \tau}+U\frac{\partial V}{\partial X}+V\frac{\partial V}{\partial Y}=-\frac{\partial P}{\partial Y}+\frac{1}{Re}\left[\frac{\partial^2 V}{\partial X^2}+\frac{\partial^2 V}{\partial Y^2}\right] \tag{3}$$

$$\frac{\partial \theta}{\partial \tau}+U\frac{\partial \theta}{\partial X}+V\frac{\partial \theta}{\partial Y}=\frac{1}{Pe}\left[\frac{\partial^2 \theta}{\partial X^2}+\frac{\partial^2 \theta}{\partial Y^2}\right] \tag{4}$$

and the associated initial and boundary conditions are

for $\tau = 0$

$$\text{at } X\to-\infty,\quad U=6(Y-Y^2),\quad V=0,\quad \theta=0 \tag{5}$$

for $\tau > 0$

$$\text{at } X\to-\infty,\quad U=6(Y-Y^2),\quad V=0,\quad \theta=0 \tag{6}$$

$$\text{at } X\to\infty,\quad \frac{\partial U}{\partial X}=0,\quad V=0,\quad \frac{\partial \theta}{\partial X}=0 \tag{7}$$

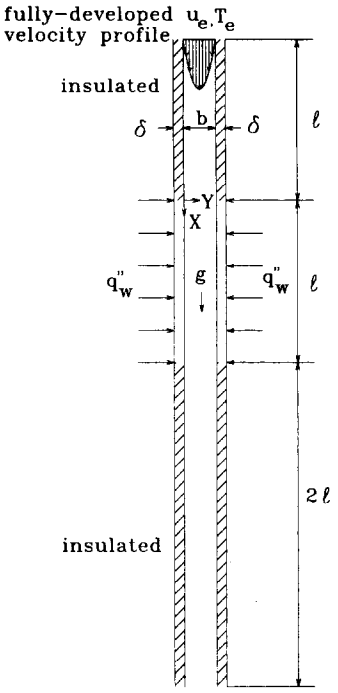

FIG. 1. Schematic diagram of the physical system.

at $Y = 0$, $U = V = 0$,

$$A\frac{\partial\theta}{\partial\tau} - \frac{\partial\theta}{\partial Y} = \begin{cases} 1 & \text{for } 0 \leqslant X \leqslant L \\ 0 & \text{otherwise} \end{cases} \quad (8)$$

at $Y = 1$, $U = V = 0$,

$$A\frac{\partial\theta}{\partial\tau} + \frac{\partial\theta}{\partial Y} = \begin{cases} 1 & \text{for } 0 \leqslant X \leqslant L \\ 0 & \text{otherwise} \end{cases} . \quad (9)$$

Note that in the opposing mixed convection the parameter Gr/Re^2, which signifies the relative strength of the buoyancy to inertia forces, is negative. The above equations are written in terms of the following nondimensional variables:

$$X = x/b, \quad Y = y/b, \quad L = l/b$$

$$U = u/\bar{u}_e, \quad V = v/\bar{u}_e, \quad \tau = t/(b/\bar{u}_e)$$

$$\theta = (T - T_e)/(q''b/k), \quad P = p/\rho\bar{u}_e^2$$

$$Re = \bar{u}_e b/\nu, \quad Gr = g\beta q''_w b^4/(k\nu^2)$$

$$Pr = \nu/\alpha, \quad A = \frac{\rho_w c_{pw}\delta}{\rho c_p b} Re\, Pr. \quad (10)$$

In the above formulation, heat capacity in the channel wall is included in equations (8) and (9) because it is important in the transient heat transfer processes, as evident from the studies of Succec [29], Lin and Kuo [30] and Joshi [31] for transient forced and free convection. The local and space-averaged Nusselt numbers on the left and right channel walls can be evaluated from the equations

$$Nu_L = \frac{h_L b}{k} = \frac{-k\left.\frac{\partial T}{\partial y}\right|_{y=0}}{T_w - T_e}\frac{b}{k} = -\frac{1}{\theta}\left.\frac{\partial\theta}{\partial Y}\right|_{Y=0}, \quad (11)$$

$$Nu_R = \frac{h_R b}{k} = \frac{k\left.\frac{\partial T}{\partial y}\right|_{y=b}}{T_w - T_e}\frac{b}{k} = \frac{1}{\theta}\left.\frac{\partial\theta}{\partial Y}\right|_{Y=1}, \quad (12)$$

and

$$\overline{Nu} = \frac{1}{L}\int_0^L Nu\, dX. \quad (13)$$

SOLUTION METHOD

Since the flow governed by equations (1)–(4) is known to be parabolic in time but elliptic in space, the solution for the problem can only be marched in time, and iterative procedures must be employed to obtain the solution in the spatial domain. The projection method developed by Chorin [32] and Temam [33] was chosen to numerically solve the time-dependent governing equations in their primitive form on a staggered grid. This fractional step method consists of two steps. First, a provisional value $\vec{V}^*$ is explicitly computed for velocity field ignoring the pressure gradient,

$$\frac{\vec{V}^* - \vec{V}^n}{\Delta\tau} + (\vec{V}^n\cdot\nabla)\vec{V}^n - \frac{1}{Re}\nabla^2\vec{V}^n - \vec{B} = 0 \quad (14)$$

where $\vec{B}$ is the buoyancy force. Then, the provisional velocity field $\vec{V}^*$ is corrected by including the pressure effect and by enforcing the mass conservation at time step $n+1$

$$\frac{\vec{V}^{n+1} - \vec{V}^*}{\Delta\tau} + \nabla P^{n+1} = 0 \quad (15)$$

and

$$\nabla\cdot\vec{V}^{n+1} = 0. \quad (16)$$

Substituting equation (16) into equation (15) yields the Poisson equation for pressure

$$\nabla^2 P^{n+1} = \frac{1}{\Delta\tau}\nabla\cdot\vec{V}^*. \quad (17)$$

In discretizing the above equations, centered difference is used to approximate all the derivatives except the convective terms. To enhance numerical stability and to yield accurate results for the complicate flow and thermal evolution studied here, a third-order upwind scheme developed by Kawamura *et al.* [34] is employed to discretize these convective terms. For instance, in the X-direction momentum equation, one of the nonlinear terms is written as

$$f\left.\frac{\partial U}{\partial X}\right|_i = f_i\frac{-U_{i+2}+8U_{i+1}-8U_{i-1}+U_{i-2}}{12\Delta X}$$

$$+|f_i|\frac{U_{i+2}-4U_{i+1}+6U_i+6U_i-4U_{i-1}+U_{i-2}}{4\Delta X}. \quad (18)$$

The first-order Euler explicit scheme was employed since it was easy to implement. It has a much lower computational cost per time step, and requires much less computer memory allocation than any equivalent implicit implementation. We also found that the first-order scheme was sufficiently accurate to resolve the smallest physical time scale. The stability of the scheme, limited by the requirement that the Courant number be less than unity (Anderson *et al.* [35]), was found to be governed by the grid spacing normal to the confined walls. The step selected to comply with the above stability limitation was smaller than that required to resolve the highest frequency which appears in the flow considered. The sequence of numerical operations are as follows:

(1) explicitly calculate $\vec{V}^*$ from equation (14);

(2) solve the pressure equation (17) for P^{n+1} by the Fast Fourier Transform (FFT) method (Wilhelmson and Erichsen [36]). This direct solution method is relatively accurate and, in fact, it was noted that the mass imbalance for every computational cell compared with the inlet mass flowrate is all below 10^{-7}. Furthermore, the residual for each discretized equation for each node is found to be less than 10^{-7};

(3) explicitly calculate the desired velocity field at the new time step, $\vec{V}^{n+1}$, from equation (15).

Various schemes were used to discretize the energy equation. The power-law scheme developed by Patankar [37] was found to be most satisfactory with the time derivative treated implicitly. By employing the Conjugate Gradient Squared method (Sonneveld [38]) to solve the resulting finite-difference equations, the temperature field at every time step can be calculated with a very high accuracy. In the computation, the convergence criterion that the relative error in temperature between two consecutive iterations is below 10^{-8} and the residual for the discretized energy equation is below 10^{-5} are enforced for every node at every time step. This method of solving the energy is further supported by noting that the overall energy balance for the channel is satisfied within 0.1%.

Due to the elliptical nature of the flow, an extended computational domain was employed, including the directly heated section ($0 \leqslant X \leqslant L$) and the insulated sections immediately upstream and downstream of it, as depicted in Fig. 1. The extended domains in the insulated sections must be long enough so that the obtained solution is independent of their sizes. In the program test, it was observed that over the ranges of the governing parameters to be considered, the upstream and downstream extended regions should each have length L and $2L$. A uniform grid system is placed in the whole computational domain. In the X-direction, 360 grid lines are used, while in the Y-direction, 32 grid lines are employed. The computation is started immediately after the sudden imposition of the heat fluxes on the channel wall at $\tau = 0$. It is terminated when the steady state is reached, which is detected by the relative changes in U, V and θ over 1000 time steps being less than 10^{-5}. For the cases without a steady state at high Gr/Re^2, the basic equations are integrated until the statistical characteristics are well developed.

Table 1. Comparison of local velocity U, temperature θ and average Nusselt number fluctuations and frequency for various grid arrangements at $Y = 0.141$ for $Re = 500$ and $Gr/Re^2 = -6$

		Grids			
	X	280×32	360×32	420×32	360×40
U	5	−1.149†	−1.389	−1.438	−1.391
		1.526‡	1.887	1.950	1.896
	10	−1.130	−1.279	−1.377	−1.297
		1.997	2.270	2.378	2.282
θ	5	2.162	2.136	2.110	2.137
		2.440	2.419	2.395	2.420
	10	4.080	4.053	4.042	4.054
		4.160	4.143	4.133	4.144
$\overline{Nu}$		0.540	0.553	0.558	0.553
		0.562	0.571	0.575	0.572
Frequency		0.345	0.360	0.368	0.357

†, ‡: minimum and maximum values during a cycle.

Considering the complicated fluid flow to be simulated here, a stringent program test is conducted. First, the predicted velocity profile at the exit of the computational domain ($X = 3L$) where the buoyancy exhibits negligible effects agrees with the exact fully developed velocity profile $U = 6(Y - Y^2)$ to the six digits after the decimal point. Then, it is observed that the predicted steady fully developed velocity profiles for a long heated section ($L \geqslant 50$) differ from the exact solution of Lavine [14] by less than 1%. Finally, a grid test is carried out. The results for a typical case are listed in Table 1. Reasonable agreement between the results for U and θ at several locations and the average Nusselt number and oscillatory frequency from various grids is noted. The 360×32 grid is therefore considered to be suitable for the present study and will be used in the subsequent computations. For the sake of accuracy, 420×32 grid lines are used for the high buoyancy cases. Regarding the effect of the time step, only a small difference in the predicted results is found when the time step is reduced by a half. The above program test indicates that the adopted solution procedures are suitable for the present study.

ONSET OF INSTABILITY

To investigate the flow stability mentioned earlier, a linear stability analysis was carried out for the limiting case of the heated section being relatively long. In this limiting case, the analytic fully developed velocity and

temperature distributions given by Lavine [14] can be used for the basic flow (U_b, V_b and θ_b). The procedures adopted here resemble those used by White [20]. The disturbance equation is obtained by subtracting the equations for the basic flow from the instantaneous flow equations, and then elminating the pressure from the resulting equations. Neglecting the nonlinear terms and assuming the disturbances as two-dimensional with the general from

$$\phi' = \hat{\phi}(Y)\exp(ik_1(X-c\tau)) \tag{19}$$

where i, k_1 and c are, respectively, the square root of -1, wave number and complex wave speed, one arrives at the equations governing the amplitudes of the Y-component disturbed velocity $\hat{V}$ and temperature $\hat{\theta}$

$$\frac{d^4\hat{V}}{dY^4} - 2k_1^2\frac{d^2\hat{V}}{dY^2} + k_1^4\hat{V} + ik_1\,Re \times\left(k_1^2U_b\hat{V} + \frac{d^2U_b}{dY^2}\hat{V} - U_b\frac{d^2\hat{V}}{dY^2} - \frac{Gr}{Re^2}\hat{\theta}\right) = ick_1\,Re\left(k_1^2\hat{V} - \frac{d^2\hat{V}}{dY^2}\right) \tag{20}$$

$$\hat{V}\,Pe\frac{d\theta_b}{dY} + i\frac{Pe}{k_1}\frac{d\theta_b}{dX} - \frac{d^2\hat{\theta}}{dY^2} + k_1^2\hat{\theta} + ik_1U_b\,Pe\,\hat{\theta} = ik_1c\,Pe\,\hat{\theta} \tag{21}$$

subject to the boundary conditions

$$\hat{V}(0) = \hat{V}(1) = \frac{d\hat{V}(0)}{dY} = \frac{d\hat{V}(1)}{dY} = 0$$

$$\frac{d\hat{\theta}(0)}{dy} = \frac{d\hat{\theta}(1)}{dY} = 0. \tag{22}$$

The above eigenvalue problem was solved by expressing $\hat{V}$ and $\hat{\theta}$ as the Nth degree Chebychev polynomials and then discretize the equations by the collocation method (Canuto *et al.* [39]). The resulting eigenmatrix is solved by the IMSL subroutine EIGZC. The above procedure was first tested for the limiting case of the Orr–Sommerfeld equation (Orszag [40]). Excellent agreement is noted.

The predicted neutral stability curves are shown in Fig. 2 for fluid with $Pr = 0.01$ flowing in a long heated channel with the Reynolds number ranging from 100 to 500. Note that the region on the left of a given curve is unstable for that case. The results indicate that the critical $|Gr/Re^2|$ decreases with increasing Reynolds number. These critical values are much smaller than the value of critical $|Gr/Re^2|$ for the appearance of flow oscillations from directly solving equations (1)–(4), as will become clear later. These differences can be attributed to the finite heated section length in the direct numerical simulation and to the fact that the lower bound is predicted in the linear stability analysis (White [20]).

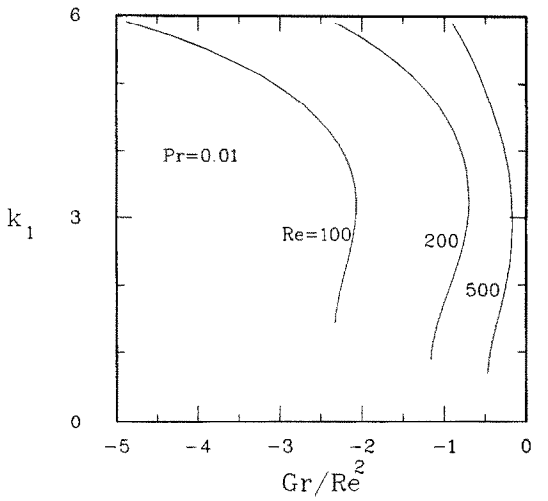

FIG. 2. Neutral stability curves for $Pr = 0.01$ with Re varied from 100 to 500.

RESULTS AND DISCUSSION

The foregoing formulation obviously indicates that the transient mixed convection in the vertical channel is governed by five nondimensional parameters. In this study, attention is focused on the effects of the Reynolds number and buoyancy-to-inertia ratio with the length of heated section L, Prandtl number Pr and wall-to-fluid heat capacity ratio A, respectively fixed at 10, 0.01 and 0. Both steady and unsteady mixed convection will be presented. Flow is steady at low buoyancy. Unsteady oscillatory flow prevails as Gr/Re^2 exceeds certain critical value.

Steady flow

Results are first demonstrated for the flow at low buoyancy. Physically, it is expected that immediately after the sudden imposition of a constant heat flux on the channel walls at $\tau = 0$, the initially fully developed velocity profile is modified by the opposing buoyancy with the near wall flow decelerated and core flow accelerated. The temporal evolution of the flow and thermal fields for a typical case at low buoyancy is shown in Fig. 3 through plotting the streamlines and isotherms at selected time instants. The plotted stream functions are -0.02, -0.01, 0.2, 0.4, 0.6, 0.8, 1.01 and 1.02 and the isotherms are 1.0, 2.0, 3.0 and 4.0. In the early transient, the development of the isotherms close to the heated plate resembles that in boundary layer flow. However, its transverse diffusion is much greater than that of the fluid with a moderate Prandtl number owing to the high thermal diffusivity for a low-Pr fluid. So in a short time, the boundary layers over the heated plates merge (as shown in Fig. 3 with $\tau = 4.0$ and 8.0). The distortion of the streamlines is slight and only observed downstream. At $\tau = 12$ a symmetric pair of weak recirculating cells are formed near the lower end of the heated section. When the steady state is reached as $\tau \geqslant 30$, the cells are larger

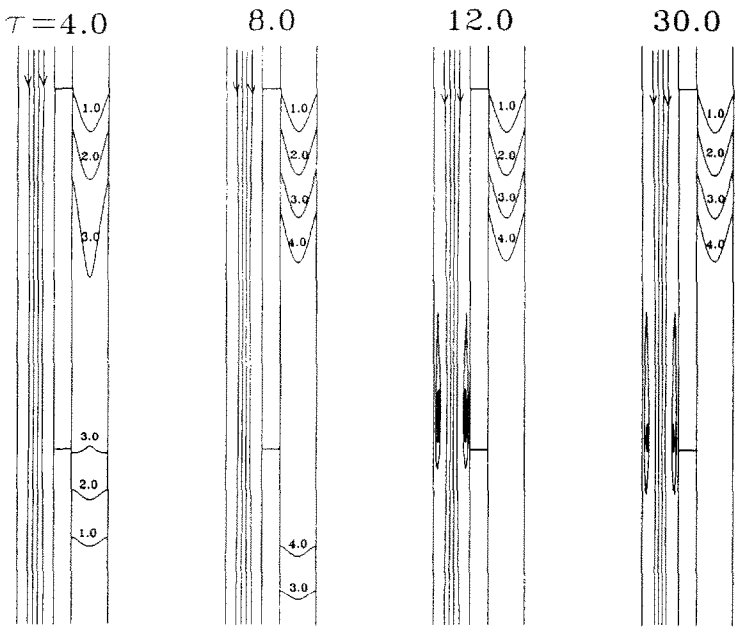

FIG. 3. Streamlines and isotherms at $\tau = 4.0$, 8.0, 12.0 and 30.0 with $Re = 800$ and $Gr/Re^2 = -1.0$.

but are still weak. These contours suggest that the transport of energy is only slightly affected when the flow is significantly modified by the buoyancy.

The time variations of the velocity and temperature profiles at the exit end of the heated section ($X = L$) are plotted in Figs. 4(a) and (b) to illustrate the strength of the flow reversal and temperature non-uniformity. The results indicate that at $\tau = 12$ the reverse flow is already well developed. Moreover, the development of steady velocity and temperature profiles from the inlet to the outlet of the heated section is shown in Figs. 4(c) and (d) for $Re = 800$ and $Gr/Re^2 = -1.0$. At the inlet ($X = 0$) the fluid still flows unidirectionally downwards. Then at $X = 1.67$ the near-wall flow is almost stagnant and the velocity gradient normal to the wall is close to zero, indicating the vanishing viscous shear force. Besides, a significant velocity increase is noted in the mid-part of the channel. Further downstream, a reverse flow appears in the near-wall region which strengthens in the downward direction. The steady temperature distribution is only slightly affected by the presence of the flow reversal. In fact, for $X > 1.67$ the $(\theta - \theta_b)$ curves at adjacent positions differ from each other by a constant value, reflecting that thermally fully developed condition is already reached for $X > 1.67$. However, the flow is not hydrodynamically developed because the heated section length is finite, unlike that considered by Lavine [14].

After depicting the time evolution of the flow and heat transfer the effects of Gr/Re^2 and Re on the steady temperature and velocity distributions are discussed. The effect of Gr/Re^2 is examined first. The temperature and velocity distributions at the outlet of the heated section are shown in Figs. 5(a) and (b) with $Re = 500$. The results indicate that the outlet temperature increases slightly with the magnitude of Gr/Re^2 (Fig. 5(a)). We believe that this results from the stronger reverse flow at higher Gr/Re^2. The flow remains unidirectional when $|Gr/Re^2|$ is below 0.6. The recirculating cell is larger at larger opposing buoyancy. In our calculations the steady state does not exist if $|Gr/Re^2|$ is above 1.2 with $Re = 500$. Next, the effect of the Reynolds number are examined in Figs. 5(c) and (d). In the figures, the corresponding Gr is also indicated. The effect of the Reynolds numbers is rather pronounced, especially for the velocity profiles. Note that the reverse flow is stronger for a high Reynolds number case with Gr/Re^2 fixed. The results in Fig. 5 clearly indicate that both Gr/Re^2 and Re have substantial influence on the mixed convection flow. This is very different from the mixed convection channel flow at lower buoyancy in which no flow reversal occurs, and the flow is uniquely determined by the parameter Gr/Re (Aung [2]). A suitable mixed convection parameter for a recirculating developing mixed convection flow in a vertical channel remains to be found.

Oscillatory flows

In this section, we describe the situation when the buoyancy force is high enough to exceed the critical Gr/Re^2 so that the flow becomes oscillatory. As the critical Gr/Re^2 is slightly exceeded, a periodic motion with a fundamental frequency and its harmonics is noted. With further increase in Gr/Re^2, a second fundamental frequency sets in and a quasi-periodic flow is therefore obtained. It is of interest to point out that

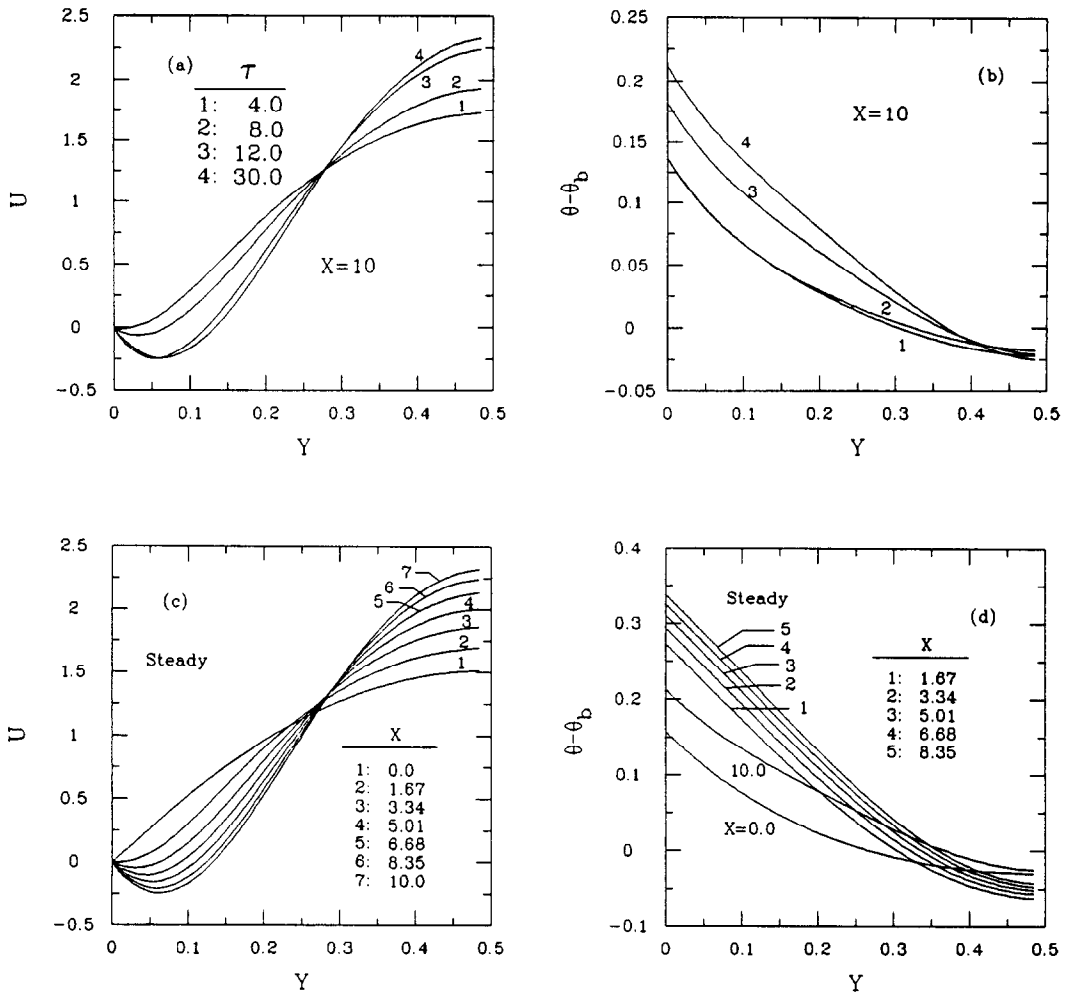

FIG. 4. Velocity (a) and temperature (b) profiles at the exit end of the heated section at several time instants; steady velocity (c) and temperature (d) profiles at various axial locations for $Re = 800$ and $Gr/Re^2 = -1$.

in the initial transient, the flow is symmetric with respect to the center plane $Y = 1/2$, but at a certain later time, sudden flow and thermal asymmetries take place, suggesting the occurrence of the symmetry breaking process which is frequently seen in many nonlinear dynamic systems [41].

Before describing the statistical characteristics of the oscillatory flow, we first illustrate the flow evolution for a case with periodic oscillation in Fig. 6 for $Gr/Re^2 = -3$ and $Re = 500$. The stream functions are -0.2, -0.1, 0.2, 0.4, 0.6, 0.8, 1.1 and 1.2. The isotherms are 1.0, 2.0, 3.0 and 4.0 hereafter. Initially, at small τ, the opposing buoyancy induces a symmetric pair of elongated cells in the heated section. These cells grow and become more elongated and finally disintegrate, as seen at $\tau = 12.182$. Flow and thermal asymmetry is noted a little later ($\tau = 18.79$). This breaking in symmetry can be attributed to the nonlinear evolution of the extremely small asymmetry in the random disturbance added at the inlet. The cell disintegration and symmetry breaking processes gradually propagate upstream. After a certain period of transient irregular oscillation, a period flow is formed at large τ. Figure 6 shows a few snapshots of this periodic flow for $\tau = 80.298 \sim 83.428$. The gross structure of the flow is characterized by a sinuous flow stream in the central part of the channel accompanied by a number of small recirculations adjacent to the walls. This resembles the flow in unstable plane mixing layer.

To reveal the detailed fluctuation characteristics at large times, the time records of the axial velocity and temperature at two selected locations along with the average Nusselt numbers for the right and left plates are presented in Fig. 7 for $Re = 500$ and $Gr/Re^2 = -3$. Also included in this figure are the

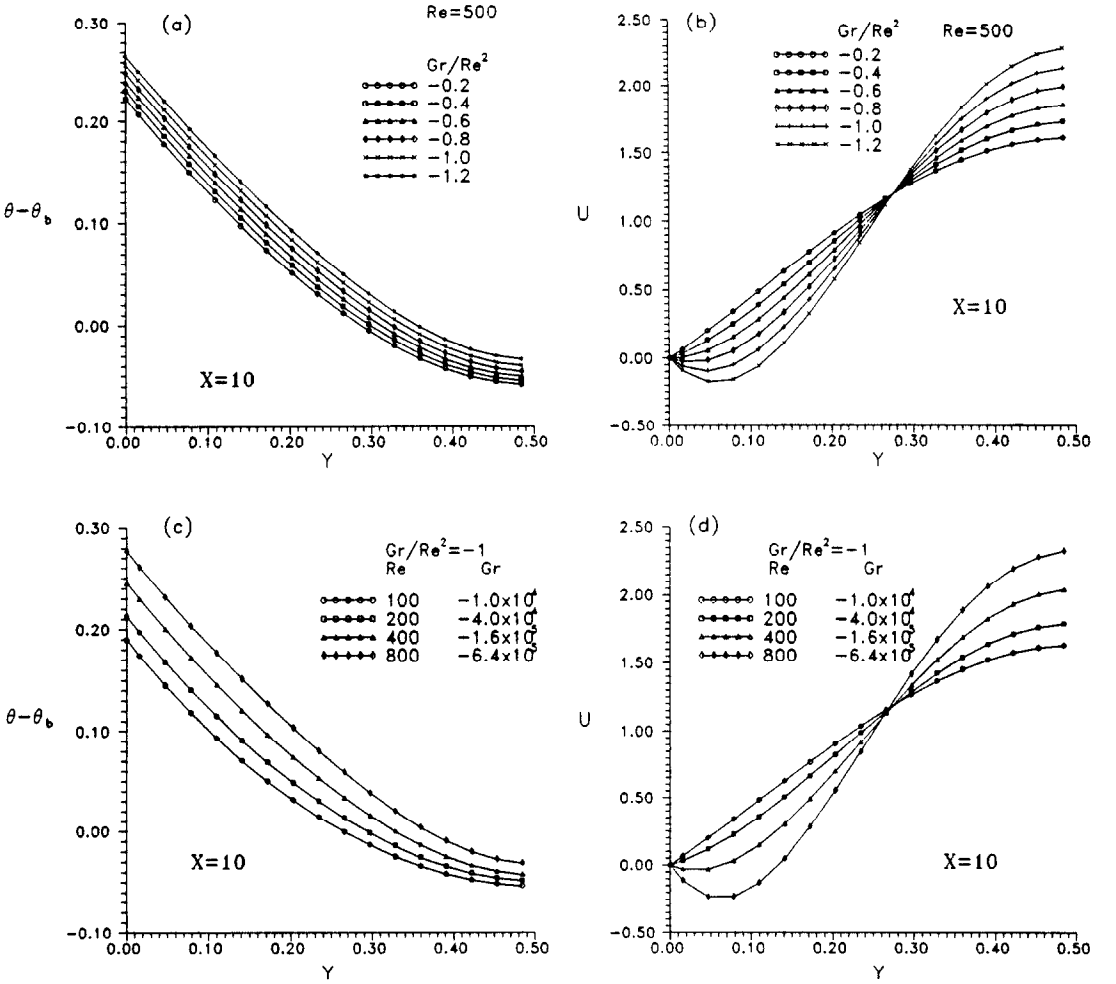

FIG. 5. The effects of Gr/Re^2 and Re on the temperature ((a) and (c)) and velocity ((b) and (d)) distributions at the exit end of the heated section.

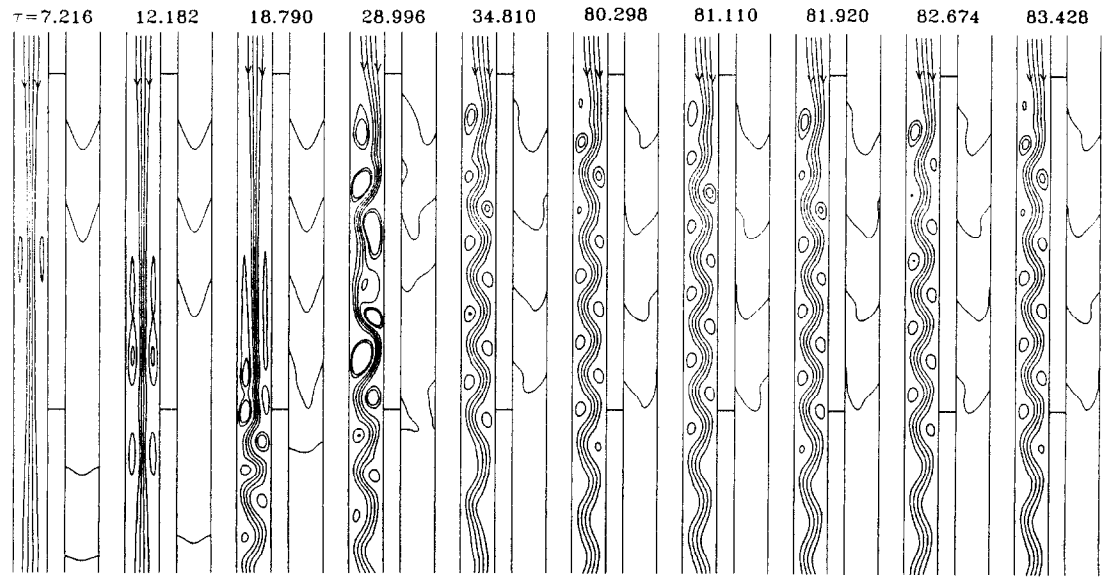

FIG. 6. Streamlines and isotherms in the flow for $Re = 500$ and $Gr/Re^2 = -3$.

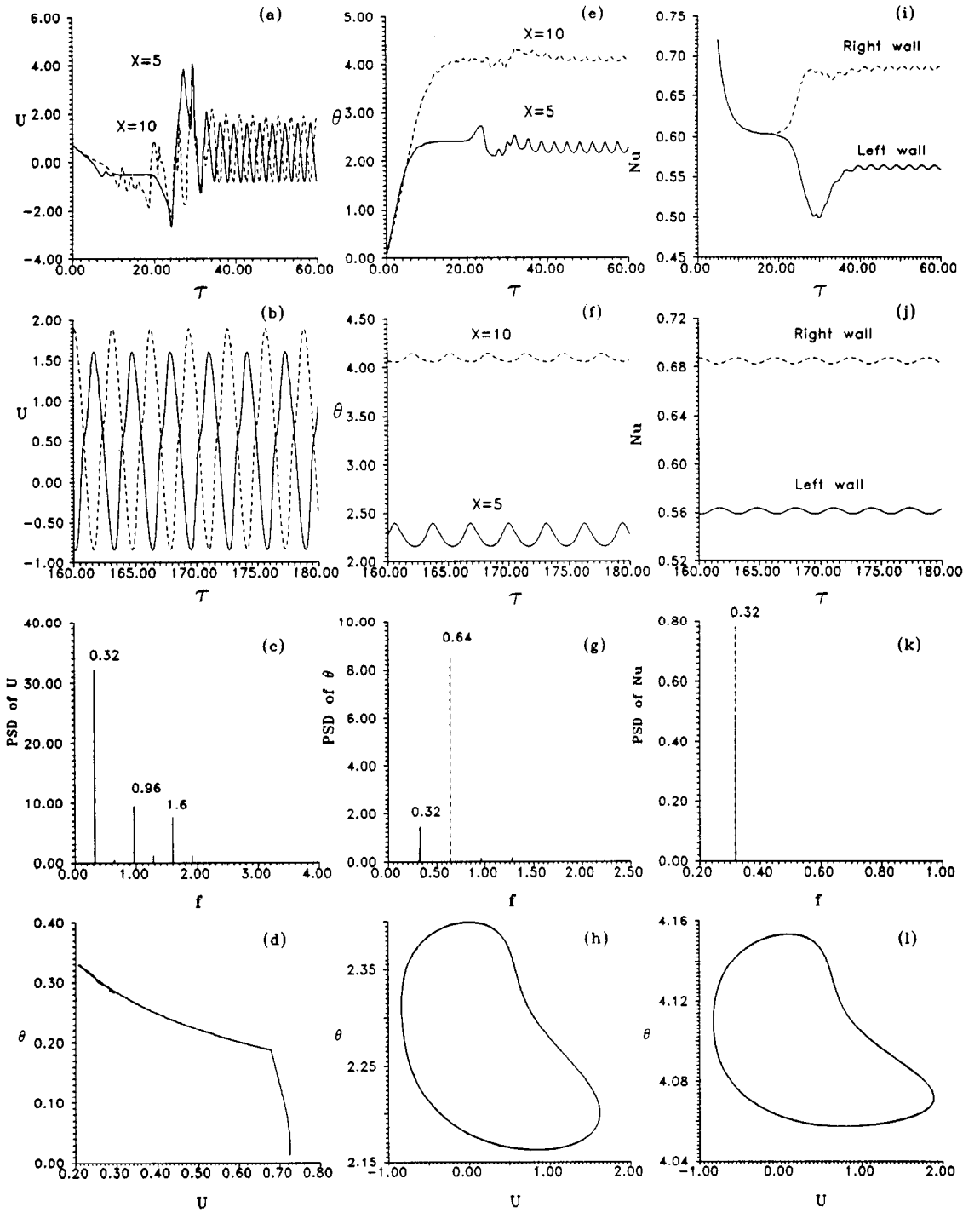

FIG. 7. Initial transient, periodic evolution and power spectral densities for velocity and temperature at selected locations and the average Nusselt numbers; (d), (h) and (l) illustrate the phase space trajectories at $X = 0$, 5 and 10 at $Y = 0.141$ for $Re = 500$ and $Gr/Re^2 = -3$.

corresponding power spectral densities and phase trajectories of U vs θ. The results in Figs. 7(a), (b), (e) and (f) indicate that the amplitude of the velocity oscillation is larger at the exit end of the heated section ($X = 10$), while larger oscillation amplitude in temperature is noted at the middle section ($X = 5$). This is the direct consequence of the quick establishment of the temperature field in the low-Pr fluid due to its high thermal diffusivity. Thus, the fluctuation in buoyancy force dwindles in the downward direction. The periodic motion is reflected by the sharp peaks in the power spectral densities. Specifically, there is one fundamental frequency at 0.32 and its harmonics with $f = 0.64$, 0.96, and 1.6. The periodic flow is further manifested by the single closed curve in the phase diagram (Figs. 7(h) and (l)). The closed curve is denoted as a limit cycle in the study of nonlinear dynamic systems. The flow asymmetry discussed earlier is quantitatively illustrated by the unequal space-averaged Nusselt numbers for the left and right plates in Figs. 7(i) and (j). Finally, the flow at the inlet of the heated section, which reaches a steady state, is indicated by the presence of a limiting point in the phase diagram (Fig. 7(d)).

Effects of the buoyancy-to-inertia strength are now examined. An increase of Gr/Re^2 from -3 to -9 causes an earlier appearance of the flow oscillation and asymmetry. Besides, the oscillation frequency and amplitude is larger for a higher Gr/Re^2. In fact, the fundamental frequency increases from 0.32 for $Gr/Re^2 = -3$ to 0.362 for $Gr/Re^2 = -6$. An inspection of flow formation discloses that the asymmetry appears at the same time over the entire heated section. However, with a lower Gr/Re^2, the symmetry breaking starts at the exit end ($X = 10$). The two cases can be classified into two different kinds of symmetry breaking. Finally, it is interesting to note that the temperature increase is concentrated in the entry region of the heated section.

Figure 8 presents the results for an even higher buoyancy strength ($Gr/Re^2 = -12$) at large τ when the initial transient has died out. Note that the flow is quasi-periodic at this Gr/Re^2 with the presence of two fundamental frequencies, $f = 0.0875$ and 0.199. The other peaks in the power spectral density are the harmonics of the fundamental modes resulting from the period-doubling mechanism [42, 43], as evident from Table 2. The harmonics are the linear combination of the fundamental modes. The corresponding U vs θ phase diagram is no longer a single closed curve; even more, no obvious repetition is noted. The trajectories are similar to each other but never repeat. It is hard to precisely determine the margin of transition from single frequency to the two-frequency periodic motion. But in our calculation, we find that the second fundamental frequency sets in at Gr/Re^2 about -9 with $Re = 500$.

A further increase of Gr/Re^2 to -20 causes the flow to become nonperiodic from examining the time records of the velocity and temperature. Characteristics of the complicated aperiodic oscillations can be understood by checking the power spectral density in Fig. 9. Comparing the result in Fig. 9(b) with that for $Gr/Re^2 = -12$ indicates that for $Gr/Re^2 = -20$ the oscillations shift to lower frequencies with two fundamental modes at $f = 0.085$ and 0.142. Other frequencies can be represented by the linear combination of these two modes (Table 2). Besides, the peaks in Fig. 9(b) are broadbanded, reflecting that the flow is transitional.

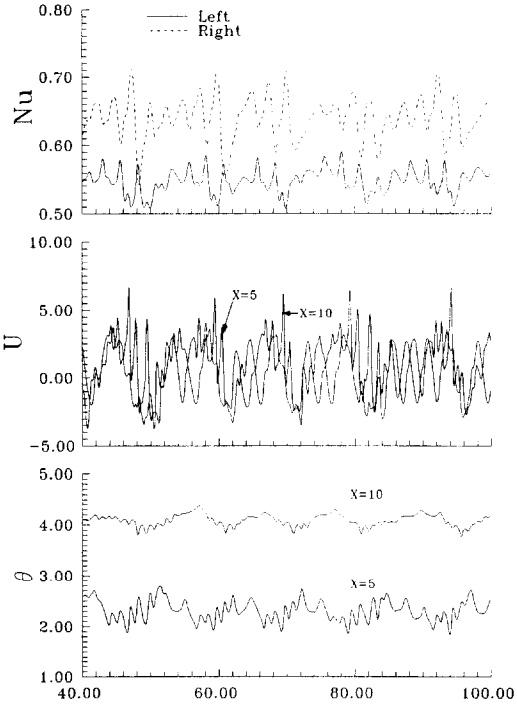

FIG. 8. Time traces of $\overline{Nu}$, U and θ for $X = 5$ and 10 at $Y = 0.141$ with $Re = 500$ and $Gr/Re^2 = -12$.

Now the effects of the Reynolds number are considered. The time variations of U and θ at two selected locations and $\overline{Nu}_L$ and $\overline{Nu}_R$ are shown in Fig. 10 for $Re = 1600$ and $Gr/Re^2 = -3$. Contrasting these results with those in Fig. 7 for $Re = 500$ and $Gr/Re^2 = -3$ indicates that at $Re = 1600$ the symmetric oscillation persists for a longer period before symmetry breaking appears. A close inspection of the

Table 2. The fundamental and harmonic frequencies and their relations for $Gr/Re^2 = -12$ and -20

$Gr/Re^2 = -12$			$Gr/Re^2 = -20$		
f	C_1	C_2	f	C_1	C_2
0.0875	1	0	0.0513	$-2/5$	3/5
0.144	1/2	1/2	0.085	1	0
0.199	0	1	0.142	0	1
0.311	2	-1	0.195	9/5	3/10
0.394	0	2	0.257	0	3
0.488	1	1	0.325	$-9/2$	5

Note: $f = C_1 f_1 + C_2 f_2$, where f_1 and f_2 are, respectively, the first and second fundamental frequencies.

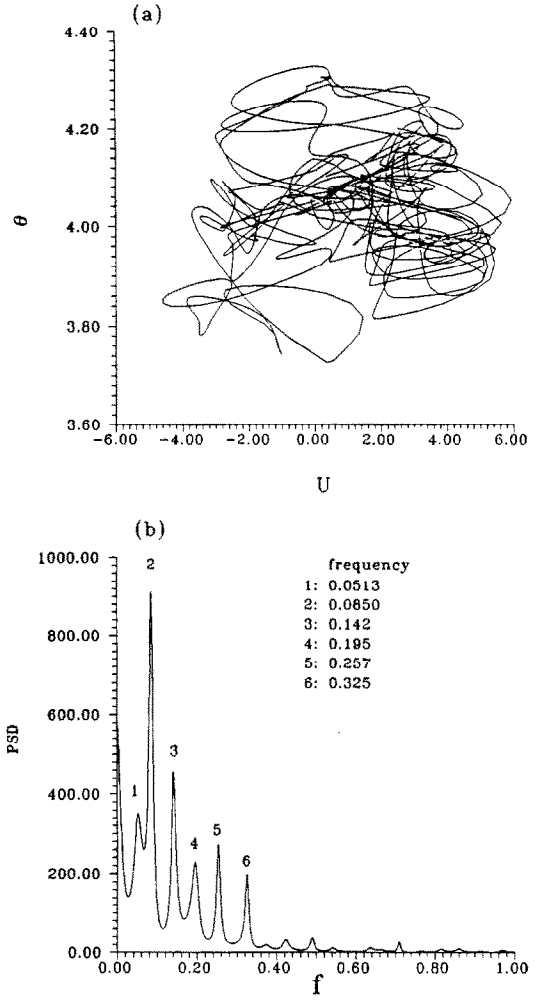

FIG. 9. Phase space trajectory of U vs θ and power spectral density of U at $X = 10$, $Y = 0.141$ with $Re = 500$ and $Gr/Re^2 = -20$.

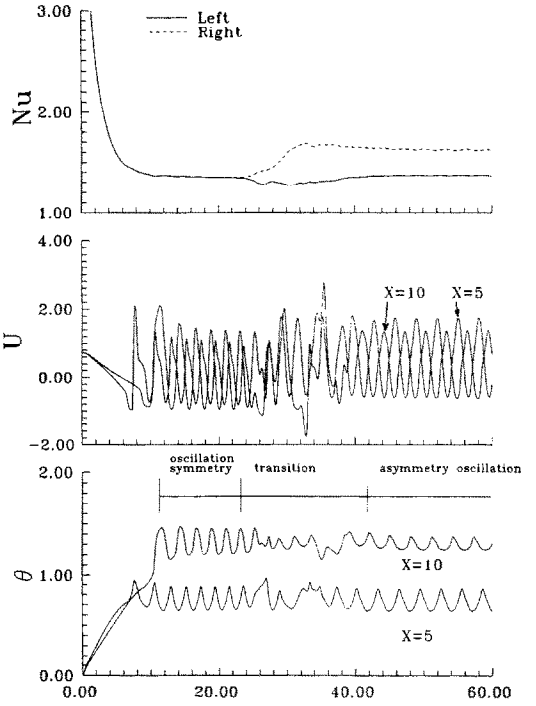

FIG. 10. Time traces of $\overline{Nu}$, U and θ for $X = 5$ and 10 at $Y = 0.141$ with $Re = 1600$ and $Gr/Re^2 = -3$.

results suggests that the transient response can be roughly divided into three stages, i.e. symmetric periodic oscillation, transition (or symmetry breaking as used earlier) and asymmetric periodic oscillation stages. At $Re = 500$, the symmetric periodic oscillation stage does not exist (Fig. 7(a)). Checking the flow evolution reveals that the cells grow and are symmetrically broken with respect to the plane $Y = 1/2$ in the longitudinal direction during the symmetric oscillation stage. The greater the inertia force, the longer this stage. Immediately after the symmetric oscillation stage, small asymmetric disturbances are found throughout the domain. Then the symmetric flow is simultaneously broken down. Through an adjustment stage, we name it the transition stage, the asymmetric periodic flow is established. We only find a fundamental frequency when the Reynolds number is increased from 500 to 1600 as we already noted. However, only a slight difference is noted for the fundamental frequency after the periodic state is reached. The magnitude of the oscillation increases with the Reynolds number.

Finally, we represent the relationship of the effective heat transfer coefficient for the entire heated section vs the opposing buoyancy at large τ with $Re = 500$. Since $\overline{Nu}_L$ may not be equal to $\overline{Nu}_R$, we define the effective heat transfer coefficient $\overline{Nu}$ as the average of $\overline{Nu}_L$ and $\overline{Nu}_R$. The states which possess no oscillation (i.e. steady), one and two fundamental frequencies are clearly distinguished by the dramatic changes of slopes in the curve.

CONCLUSION AND REMARKS

The buoyancy and inertia effects on a low Prandtl fluid flowing through a symmetrically and uniformly heated vertical plane channel is numerically investigated. Linear stability theory was carried out and the opposing buoyancy is found to dramatically destabilize the flow. Then, numerical results were presented particularly to illustrate the temporal evolution of the flow and heat transfer for stable and oscillatory situations. In addition, characteristics of the velocity and temperature fluctuations were examined in detail. The main results can be summarized as follows:

(1) There exists a critical Gr/Re^2 for a specified Reynolds number. Stable flow results if $|Gr/Re^2| < |Gr/Re^2|_{critical}$. Otherwise we find an oscillatory flow.

(2) After exceeding $|Gr/Re^2|_{critical}$, a fundamental

frequency sets in. Then two fundamental frequencies appear if Gr/Re^2 is high enough.

(3) The inertia force stabilizes the flow, but the opposing buoyancy has a reverse effect.

(4) Symmetric and asymmetric oscillations are both possible in different transient stages.

For a much higher Gr/Re^2 (say, $Gr/Re^2 = -30$), the two-dimensional formulation is questionable since the flow becomes transitional and three-dimensional. This area is still left to be solved.

Acknowledgement—The financial support of this study by the engineering division of National Science Council of Taiwan, R.O.C., through contract NSC78-0401-E009-11 is greatly appreciated.

REFERENCES

1. T. S. Chen and B. F. Armaly, Mixed convection in external flow. In *Handbook of Single-Phase Convective Heat Transfer* (Edited by S. Kakac, R. K. Shah and W. Aung), Chap. 14. Wiley, New York (1987).
2. W. Aung, Mixed convection in internal flow. In *Handbook of Single-Phase Convective Heat Transfer* (Edited by S. Kakac, R. K. Shah and W. Aung), Chap. 15. Wiley, New York (1987).
3. B. Gebhart, Y. Jaluria, R. L. Mahajan and B. Sammarkia, *Buoyancy-Induced Flows and Transport*, Chap. 10. Hemisphere, Washington, DC (1988).
4. G. Muller, G. Neumann and W. Weber, Natural convection in vertical Bridgman configurations, *J. Crystal Growth* **70,** 78–93 (1984).
5. M. M. Ei-Wakil, *Power-Plant Technology*, Chaps. 11 and 13. McGraw-Hill, New York (1984).
6. L. N. Tao, On combined free and forced convection in channels, *ASME J. Heat Transfer* **82,** 233–238 (1960).
7. J. Quintiere and W. K. Mueller, An analysis of laminar free and forced convection between finite vertical parallel plates, *ASME J. Heat Transfer* **95,** 53–59 (1973).
8. L. S. Yao, Free and forced convection in the entry region of a heated vertical channel, *Int. J. Heat Mass Transfer* **26,** 65–72 (1983).
9. L. C. Chow, S. R. Husain and A. Campo, Effects of free convection and axial conduction on forced convection heat transfer inside a vertical channel at low Peclet numbers, *ASME J. Heat Transfer* **106,** 297–303 (1984).
10. W. Aung and G. Worku, Theory of fully developed combined convection including flow reversal, *ASME J. Heat Transfer* **108,** 485–488 (1986).
11. W. Aung and G. Worku, Mixed convection in ducts with asymmetric wall heat flux, *ASME J. Heat Transfer* **109,** 947–951 (1987).
12. T. Cebeci, A. A. Khattab and R. LaMont, Combined natural and forced convection in vertical ducts, *Proc. 7th Int. Heat Transfer Conference* (Edited by U. Grigull, E. Hahne, K. Stephan and J. Straub), Vol. 3, pp. 419–424 (1982).
13. W. Aung and G. Worku, Developing flow and flow reversal in a vertical channel with asymmetric wall temperature, *ASME J. Heat Transfer* **108,** 299–304 (1986).
14. A. S. Lavine, Analysis of fully developed opposing mixed convection between inclined parallel plates, *Wärme- und Stoffubertragung* **23,** 249–257 (1988).
15. D. B. Ingham, D. J. Keen and P. J. Heggs, Two dimensional combined convection in vertical parallel plate ducts, including situations of flow reversal, *Int. J. Numer. Meth. Engng* **26,** 1645–1664 (1988).
16. D. B. Ingham, D. J. Keen and P. J. Heggs, Flows in vertical channels with asymmetric wall temperatures and including situations where reversal flows occur, *ASME J. Heat Transfer* **110,** 910–917 (1988).
17. D. B. Ingham, D. J. Keen, P. J. Heggs and B. R. Morton, Recirculating pipe flows, *J. Fluid Mech.* **213,** 443–464 (1990).
18. P. J. Heggs, D. B. Ingham and D. J. Keen, The effects of heat conduction in the wall on the development of recirculating combined convection flows in vertical tubes, *Int. J. Heat Mass Transfer* **33,** 517–528 (1990).
19. A. S. Lavine, M. Y. Kim and C. N. Shores, Flow reversal in opposing mixed convection flow in inclined pipes, *ASME J. Heat Transfer* **111,** 114–120 (1989).
20. F. M. White, *Viscous Fluid Flow*, Chap. 5. McGraw-Hill, New York (1974).
21. M. A. Shadday, Jr., Combined forced/free convection through vertical tubes at high Grashof numbers, *Proc. 8th International Heat Transfer Conference* (Edited by C. L. Tien, V. P. Carey and J. K. Ferrel), Vol. 3, pp. 1433–1437 (1986).
22. G. F. Scheele, E. M. Rosen and T. J. Hanratty, Effect of natural convection on transition to turbulence in vertical pipes, *Can. J. chem. Engng* **38,** 67–73 (1960).
23. G. F. Scheele and T. J. Hanratty, Effect of natural convection on stability of flow in a vertical pipe, *J. Fluid Mech.* **14,** 244–256 (1962).
24. W. T. Lawrence and J. C. Chato, Heat transfer effects on the developing laminar flow inside vertical tubes, *ASME J. Heat Transfer* **88,** 214–222 (1966).
25. B. Zeldin and F. W. Schmidt, Developing flow with combined forced-free convection in an isothermal vertical tube, *ASME J. Heat Transfer* **94,** 211–223 (1972).
26. D. T. J. Hurle, E. Jakeman and C. P. Johnson, Convective temperature oscillations in molten Gallium, *J. Fluid Mech.* **64**(3), 565–576 (1974).
27. D. J. Knuteson, A. L. Fripp, G. A. Woodell and W. J. Debnam, Jr., Oscillation phase relations in a Bridgman system, *J. Crystal Growth* **109,** 127–132 (1991).
28. G. Muller, Convection in melts and crystal growth. In *Convective Transport and Instability Phenomena* (Edited by Jurgen Zierep and Herbert Oertel, Jr.), pp. 441–467 (1982).
29. J. Succec, Unsteady conjugated forced convective heat transfer in a duct with convection from the ambient, *Int. J. Heat Mass Transfer* **30,** 1963–1970 (1987).
30. T. F. Lin and J. C. Kuo, Transient conjugated heat transfer in fully developed laminar pipe flows, *Int. J. Heat Mass Transfer* **31,** 1093–1102 (1988).
31. H. M. Joshi, Transient effect in natural convection cooling of vertical parallel channels, *Int. Commun. Heat Mass Transfer* **15,** 227–238 (1988).
32. A. J. Chorin, Numerical solution of the Navier–Stokes equations, *Math. Comput.* **22,** 745–762 (1968).
33. R. Temam, On an approximation solution of the Navier–Stokes equations by the method of fractional step: Part 1, *Archs ration. Mech. Analysis* **32,** 135–153 (1968).
34. T. Kawamura, H. Takami and K. Kawahara, New higher-order upwind scheme for impressible Navier–Stokes equations, *Proc. 9th Int. Conf. Num. Meth. Fluid Dynm.*, Springer, pp. 291–295 (1985).
35. D. A. Anderson, J. C. Tannehill and R. H. Pletcher, *Computational Fluid Mechanics and Heat Transfer*, Chap. 4. Hemisphere, Washington, D.C. (1984).
36. R. B. Wilhelmson and J. H. Ericksen, Direct solution for Poisson's equations in three dimensions, *J. Comput. Phys.* **25,** 319–331 (1977).
37. S. V. Patanakar, *Numerical Heat Transfer and Fluid Flow*. McGraw-Hill, New York (1980).
38. P. Sonneveld, CGS, a Fast Lanczos-type solver for nonsymmetric linear systems, *SIAM J. Sci. Stat. Comput.* **10,** 36–52 (1989).
39. C. Canuto, M. Y. Hussaini, A. Quarteroni and T. A. Zang, *Spectral Methods in Fluid Dynamics*, Chap. 2. Springer, New York (1988).

40. S. A. Orszag, Accurate solution of the Orr–Sommerfeld stability equation, *J. Fluid Mech.* **50,** 689–703 (1971).
41. J. D. Crawford and E. Knobloch, Symmetry and symmetry-breaking bifurcations in fluid dynamics, *Ann. Rev. Fluid. Mech.* **23,** 341–387 (1991).
42. J. B. McLaughlin and S. A. Orszag, Transition from periodic to chaotic thermal convection, *J. Fluid Mech.* **122,** 123–142 (1982).
43. J. P. Gollub and S. V. Benson, Many routes to turbulent convection, *J. Fluid Mech.* **100**(3), 449–470 (1980).